

## Orientation mode selection mechanisms for sheared nematic liquid crystalline materials

Tomohiro Tsuji and Alejandro D. Rey\*

*Department of Chemical Engineering, McGill University, 3610 University Street, Montreal, Quebec, Canada H3A 2B2*

(Received 24 October 1997)

An extensive analysis of the flow orientation modes of sheared liquid crystalline materials is performed using a complete nonlinear nonequilibrium theory that takes into account short and long range order elasticity and viscous flow effects. It is found that there are two main orientation modes in shear flow: (i) in-plane modes, where the average molecular orientation is in the shear plane ( $\mathbf{v}$ - $\nabla\mathbf{v}$  plane, where  $\mathbf{v}$  is the velocity vector); and (ii) out-of-plane modes where the average molecular orientation has a nonzero component along the vorticity ( $\nabla\times\mathbf{v}$ ) axis. It is found that there are four in-plane orientation modes, and five out-of-plane modes, depending on the magnitude of the ratio of short to long range elasticity ( $R$ ), and the magnitude of the ratio of viscous force to long range elastic force (Ericksen number:  $Er$ ). The spatial configuration of the orientation field shows a bulk region and two boundary layers, which are smoothly and continuously connected by the action of compatibilization mechanisms. The system has two different compatibilization mechanisms at the boundary between the bulk and surface layer regions: (i) scalar order parameter adjustment, and (ii) director orientation changes. The activations of these two mechanisms are self-selected, and depend on the parametric ( $R$ ,  $Er$ ) conditions. At lower  $R$  the system easily adopts the scalar order parameter compatibilization mechanism, and at higher  $R$  and at moderate  $Er$  the system adopts the director compatibilization mechanism. Multistable nonplanar orientation modes arise in certain parametric regions. Multistability in nonplanar modes arises due to possible choices in the direction of the director escape from the shear plane (i.e., left or right), and the nucleation time of the out-of-plane orientation. These two degrees of freedom cause the appearance of chirality in the director field. The nonplanar mode selection and its chirality are stochastic, although the equations are deterministic. The complete theory unifies previously used classical theories (Doi and Leslie-Ericksen), but its predictions transcend in number and nature the predictions of the classical theories. [S1063-651X(98)05205-2]

PACS number(s): 64.70.Md, 47.50.+d, 47.54.+r

### I. INTRODUCTION

The main influences on the order and orientation of nematic liquid crystalline (LC) materials under arbitrary flows are the short range order elasticity, the long range order elasticity, and the viscous flow contribution. The short range elasticity controls the isotropic-nematic phase transition, and directly arises from the intermolecular attractive and repulsive forces such as van der Waals forces and excluded volume effects [1]. The long range order elasticity, which is the secondary effect of the intermolecular forces, transmits the surface anchoring effect from the bounding surfaces into the bulk LC materials, and is commonly known as the Frank elasticity [2]. The viscous flow contribution takes into account effect of the fluid rate of deformation and vorticity on the LC molecular field [1].

The two classical theories used to describe flow phenomena in liquid crystalline materials are the Leslie-Ericksen (LE) theory [3] and the Doi theory [4]. The LE theory is used to model, simulate, and explain flow phenomena in low molar mass nematics [3,5,6], and the Doi theory has been extensively used for polymeric nematic liquid crystals [7,8]. The two classical theories are applicable only to ideal material and flow conditions, and thus have limitations in predicting real flow phenomena. The LE theory is a vector theory that neglects the short range order elasticity, and hence it is

unable to describe changes of the scalar order parameter due to the imposition of flow or due to the presence of defects. The Doi theory is a theory based on the probability density distribution function (or tensor order parameter) that neglects the long range order elasticity, and is therefore unable to describe spatial changes due to surface anchoring conditions, defects, solitons, banded textures, and other spatially nonhomogeneous structure widely reported in the liquid crystal literature [1,9–11]. The gap between these two classical theories is a tensor theory like the Doi theory, but it also takes into account the long range elasticity, like the LE theory. A linear version of this equation was proposed and used by de Gennes many years ago [1]. Recently, Tsuji and Rey [12,13] performed an extensive analysis of a complete nonlinear model, that includes short and long range elasticities as well as viscous flow effects, for shear flow using the so-called two-dimensional (2D) planar orientation restriction; in this approximation, the eigenvector corresponding to the largest eigenvalue of the tensor order parameter is always restricted to remain in the shear plane, which is spanned by the velocity and velocity gradients directions. In that work [12,13], the limiting parametric and flow conditions that lead to the convergence of the complete theory to the classical theories were identified. In more detail, when the ratio of short range to long range elasticity is infinitely large, the complete theory becomes the LE theory, and, when the ratio of viscous flow to long range elasticity effects is also infinitely large, the complete theory becomes the Doi theory. The complete theory predicts four planar (i.e., 2D orientation

\*Electronic address: inaf@musicb.mcgill.ca

in the shear plane) flow regimes as a function of increasing shear rate. The four planar flow regimes predicted by the complete theory are modifications of the only planar solution predicted by the LE theory, and of the three spatially homogeneous planar solutions predicted by the Doi theory. The well-known [7,8] cascade of spatially homogeneous planar flow modes predicted by the Doi theory as a function of increasing shear rate encompasses (i) low shear rate director tumbling (rotation), (ii) intermediate shear rate director wagging (oscillation), and (iii) high shear rate director alignment (stationary). Since these planar modes are spatially homogeneous, there is no mechanism that can account for fixed surface anchoring in the Doi model. On the other hand, the complete model is able to describe the director bulk rotation in the presence of fixed surface anchoring by the periodic emergence of the abnormal nematic state [12,13] that smoothly and continuously connects the time dependent bulk orientation with the fixed surface orientation without the emergence of singularities. The abnormal nematic state corresponds to the nematic state, at which the two largest eigenvalues of the symmetric traceless tensor order parameter  $\mathbf{Q}$  are equal and lying on the shear plane; the abnormal nematic state was shown to emerge as a unique structure in other equilibrium processes [14]. The complete model is also able to describe the wagging oscillatory and flow alignment modes in the presence of fixed orientations. With regard to the LE theory for nonaligning nematics [15], the steady state winding solutions predicted by this theory at all shear rates [1] are, in the complete model, replaced at some critical shear rate by the tumbling-wagging composite mode if short range elasticity is dominant, or by the flow alignment mode if long range elasticity is dominant. The complete theory thus predicts different flow mechanisms, and a different number of planar flow modes than the two classical theories.

The planar flow mode approximation is unrealistic in certain situations, as demonstrated by many experiments [16–18], and by simulations using the LE theory [19–22], and the Doi theory [23,24]. The main driving forces for 3D nonplanar orientation are (i) the reduction of long range elasticity by director escape out of the shear plane, and (ii) the presence of a flow attractor along the vorticity axis.

Thus, for more realistic predictions that may lead to an explanation of ubiquitous pattern formation phenomena under shear flow [10], it is necessary to remove the planar orientation restriction and allow the effects of long range elasticity reduction by the director's escape from the shear plane, and of the flow attractor along the vorticity axis. This paper presents a comprehensive systematic study of all the solutions to the nonlinear complete model [12] for rectilinear simple shear start-up flow, in the presence of fixed planar surface director orientation, and in the absence of any orientation restrictions. The study permits one to identify, based on the planar mode results, how the nonplanar mode mechanism selects the different 3D flow modes, and in which regions of the two-dimensional parametric plane ( $Er$ - $R$  plane) the nonplanar modes are observed. These results are essential to explain the widely reported flow-induced pattern formation phenomena in polymeric liquid crystals [10,11]. The complete theory captures all the possible anisotropic viscoelastic mechanisms that promote out-of-plane orientation.

The organization of this paper is as follows. In Sec. II the

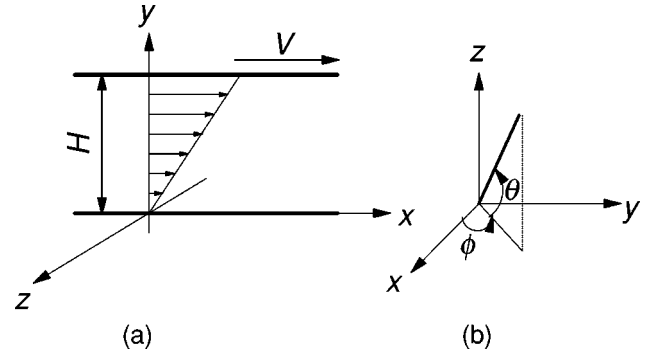


FIG. 1. (a) Definition of flow geometry and coordinate system. The plate separation is  $H$ . At time  $t=0$  the upper plate is set in motion with a known and constant velocity  $V$ , while the lower plate remains fixed. The  $x$ - $y$  plane is the shear plane, and  $z$  is along the vorticity axis. (b) Director ( $\mathbf{n}$ ) angles,  $\theta$ : twist angle;  $\phi$ : tilt angle. When  $\theta=0$  ( $\theta \neq 0$ ), the director is in a planar (nonplanar) mode.

basic equations, computational methods, dimensionless parameters, and initial and boundary conditions are presented. Section III presents the results and discussions. In Sec. III A the classification, nomenclature, main features, and approximate parametric conditions of all the planar and nonplanar flow modes predicted by the complete model are given. The out-of-plane flow modes are discussed in detail in Sec. III B. Section III C explains the origin of the multistability of flow modes. Section III D considers the generalized rheological phase diagram. The effect of elastic anisotropy is considered in Sec. III E. Finally, conclusions are presented in Sec. IV.

## II. GOVERNING EQUATIONS AND COMPUTATIONAL METHODS

To describe order in a nematic liquid crystal, we use the second order traceless symmetric tensor order parameter  $\mathbf{Q}$  [1]. An evolution equation for the tensor order parameter  $\mathbf{Q}$  is given by (see Ref. [12] for detail)

$$\begin{aligned}
 \frac{G\mathbf{Q}}{Gt} = & -\frac{6D}{(1-3/2\mathbf{Q}:\mathbf{Q})^2} \left\{ \left(1 - \frac{U}{3}\right) \mathbf{Q} \right. \\
 & - U \left[ \mathbf{Q} \cdot \mathbf{Q} - \frac{1}{3} (\mathbf{Q}:\mathbf{Q}) \delta \right] + U (\mathbf{Q}:\mathbf{Q}) \mathbf{Q} \left. \right\} + L_1 \nabla^2 \mathbf{Q} \\
 & + \frac{L_2}{2} \left\{ \nabla (\nabla \cdot \mathbf{Q}) + [\nabla (\nabla \cdot \mathbf{Q})]^T - \frac{2}{3} \text{tr}[\nabla (\nabla \cdot \mathbf{Q})] \delta \right\} \\
 & + \frac{2}{3} \beta \mathbf{A} + \beta \left\{ \mathbf{A} \cdot \mathbf{Q} + \mathbf{Q} \cdot \mathbf{A} - \frac{2}{3} (\mathbf{A}:\mathbf{Q}) \delta \right\} \\
 & - \frac{1}{2} \beta \{ (\mathbf{A}:\mathbf{Q}) \mathbf{Q} + \mathbf{A} \cdot \mathbf{Q} \cdot \mathbf{Q} + \mathbf{Q} \cdot \mathbf{A} \cdot \mathbf{Q} + \mathbf{Q} \cdot \mathbf{Q} \cdot \mathbf{A} \\
 & - [(\mathbf{A} \cdot \mathbf{Q}) : \mathbf{Q}] \delta \}, \tag{1}
 \end{aligned}$$

where  $G/Gt$  represents the corotational derivative, and  $D$ ,  $U$ ,  $L_i$  ( $i=1,2$ ),  $\eta$ , and  $\mathbf{A}$  are the rotational diffusivity coefficient, dimensionless nematic potential intensity, Landau co-

efficient [25], viscosity, and rate of strain tensor, respectively; the rate of strain tensor is defined by  $\mathbf{A} = \frac{1}{2}[(\nabla \mathbf{v})^T + \nabla \mathbf{v}]$  when  $\mathbf{v}$  is the velocity vector. A linear version of Eq. (1) can be found in the book by de Gennes [1].

In this paper, we study a one-dimensional rectilinear simple start-up shear flow with Cartesian coordinates, as shown in Fig. 1(a). The lower plate is fixed and the upper plate starts moving at  $t=0$  in the  $+x$  direction with a known constant velocity  $V$ ; the plate separation is  $H$ . The  $z$  axis is coaxial with the vorticity axis, and the shear plane is spanned by the  $x$ - $y$  directions. Scaling with the shear rate  $\dot{\gamma}$ , the plate distance  $H$ , and the Landau coefficient  $L_1$ , the dimensionless form of Eq. (1), is

$$\begin{aligned} \text{Er} \frac{G\mathbf{Q}}{Gt^*} = & R \left( -\frac{6}{(1-3/2\mathbf{Q}:\mathbf{Q})^2} \left\{ \left(1 - \frac{U}{3}\right)\mathbf{Q} \right. \right. \\ & \left. \left. - U \left[ \mathbf{Q} \cdot \mathbf{Q} - \frac{1}{3} (\mathbf{Q}:\mathbf{Q})\delta \right] + U(\mathbf{Q}:\mathbf{Q})\mathbf{Q} \right\} \right) + \nabla^2 \mathbf{Q} \\ & + \frac{L_2^*}{2} \left\{ \nabla(\nabla \cdot \mathbf{Q}) + [\nabla(\nabla \cdot \mathbf{Q})]^T \right. \\ & \left. - \frac{2}{3} \text{tr}[\nabla(\nabla \cdot \mathbf{Q})]\delta \right\} \\ & + \text{Er} \left( \frac{2}{3} \beta \mathbf{A}^* + \beta \left\{ \mathbf{A}^* \cdot \mathbf{Q} + \mathbf{Q} \cdot \mathbf{A}^* - \frac{2}{3} (\mathbf{A}^*:\mathbf{Q})\delta \right\} \right. \\ & \left. - \frac{1}{2} \beta \{ (\mathbf{A}^*:\mathbf{Q})\mathbf{Q} + \mathbf{A}^* \cdot \mathbf{Q} \cdot \mathbf{Q} + \mathbf{Q} \cdot \mathbf{A}^* \cdot \mathbf{Q} \right. \\ & \left. + \mathbf{Q} \cdot \mathbf{Q} \cdot \mathbf{A}^* - [(\mathbf{A}^*:\mathbf{Q})\mathbf{Q}]\delta \right\}, \end{aligned} \quad (2)$$

where  $*$  denotes a dimensionless quantity, and where the dimensionless parameter  $R$  is the ratio of short range order elasticity to long range order elasticity, and the dimensionless parameter  $\text{Er}$  is the Ericksen number which represents the ratio of viscous force to long range elastic force, as follows:

$$R = \frac{D^*}{L_1 H} \quad (3a)$$

and

$$\text{Er} = \frac{\eta H V}{L_1}. \quad (3b)$$

The commonly used Deborah number is given by

$$\text{De} = \frac{\text{Er}}{R} = \frac{\eta V H^2}{D^*}. \quad (3c)$$

For general 3D orientation conditions, the tensor order parameter  $\mathbf{Q}$  has six independent components, and in the Cartesian coordinate shown in Fig. 1,  $\mathbf{Q}$  is defined as

$$\mathbf{Q} = \begin{bmatrix} Q_{xx} & Q_{xy} & Q_{xz} \\ Q_{xy} & Q_{yy} & Q_{yz} \\ Q_{xz} & Q_{yz} & Q_{zz} \end{bmatrix}. \quad (4)$$

The tensor order parameter must satisfy the traceless condition:  $Q_{xx} + Q_{yy} + Q_{zz} = 0$ . Also, it is useful to express  $\mathbf{Q}$  in terms of eigenvectors ( $\mathbf{n}$ ,  $\mathbf{m}$ , and  $\mathbf{l}$ ) and eigenvalues ( $\mu_n$ ,  $\mu_m$ , and  $\mu_l$ ) [26]:

$$\mathbf{Q} = \mu_n \mathbf{n}\mathbf{n} + \mu_m \mathbf{m}\mathbf{m} + \mu_l \mathbf{l}\mathbf{l} \quad (5)$$

where  $\mathbf{n}$  is commonly called the director. The director can be parametrized with a tilt angle  $\phi$  and a twist angle  $\theta$ . The in-plane director angle  $\phi$  and the out-of-plane angle  $\theta$  are measured from the flow direction, on the  $x$ - $y$  and  $x$ - $z$  planes, respectively, and are shown in Fig. 1(b). At the bounding surfaces we assume that  $\mathbf{Q}$  is uniaxial, and use planar fixed anchoring condition with an equilibrium scalar order parameter, as follows:

$$\mathbf{Q}(y^*=0) = \mathbf{Q}(y^*=1) = S^{\text{eq}}(\mathbf{n}_s \mathbf{n}_s - \frac{1}{3}\delta), \quad (6)$$

and set the surface director  $\mathbf{n}_s$  parallel to the flow direction:

$$\mathbf{n}_s = \begin{pmatrix} 1 \\ 0 \\ 0 \end{pmatrix}. \quad (7)$$

In Eq. (7),  $S^{\text{eq}}$  is the equilibrium scalar order parameter, given in the Doi theory [4] by

$$S^{\text{eq}} = \frac{1}{4} + \frac{3}{4} \left( 1 - \frac{8}{3U} \right)^{1/2}. \quad (8)$$

Equation (6) indicates that the surface is treated as rigid; more complex boundary conditions that treat the surface as viscoelastic [27] are possible, but they are not used in this study due to the absence of experimental data that would warrant its need.

To compute the director's escape from the shear  $x$ - $y$  plane during shear start-up flow, it is necessary to take into account the effects of thermal fluctuations on the tensor order parameter field prior to the imposition of the shear flow, since they allow symmetry breaking with respect to the shear plane. It is important to note that performing shear start-up simulations with an initially planar director field will always yield planar director modes and miss all the relevant phenomena. Throughout this paper we refer to a director field with  $n_z=0$  as the in-plane mode, and to a director field with  $n_z \neq 0$  as the out-of-plane mode. In this work we use an infinitesimal white noise on the initial director field. Thus

$$\mathbf{Q}(0 < y^* < 1, t^* = 0) = S^{\text{eq}}(\mathbf{n}^{\text{ini}} \mathbf{n}^{\text{ini}} - \frac{1}{3}\delta), \quad (9a)$$

$$\mathbf{n}^{\text{ini}} = \begin{pmatrix} \cos(\varepsilon \xi) \\ 0 \\ \sin(\varepsilon \xi) \end{pmatrix}, \quad (9b)$$

where  $\mathbf{n}^{\text{ini}} = \mathbf{n}(t^* = 0, 0 < y^* < 1)$ ,  $\varepsilon = 10^{-4}(\pi/180)$ , and  $\xi$  is a Gaussian noise.

Throughout this work we set  $\beta = 0.9$  (see Ref. [28] for details) and  $U = 6$ . The chosen value for the Landau coefficient

cient is  $L_1 = 2L_2$  for all except explicitly mentioned cases. In the uniaxial limit of the order parameter [ $\mu_n \neq \mu_m = \mu_l$  in Eq. (5)], this can be expressed in terms of the Frank elasticity coefficient as follows:  $K_1 = 3K_2 = K_3$  [25]. The selected ranges for the dimensionless parameters  $R$  and  $Er$  are  $0 < R < 10^4$  and  $0 < Er < 10^5$ .

The fourth order Runge-Kutta method and the second order finite difference method are used for the time and space integration of Eq. (2). The computational conditions are the Runge-Kutta time step width  $\Delta t^* = 10^{-3}$ , and the spatial discretization width  $\Delta y^* = 10^{-2}$ . Convergence and validation criteria were performed using standard methods [12].

### III. RESULTS AND DISCUSSION

#### A. Solution modes and flow mechanisms

##### 1. Classification of solution modes

In this section, we define the nomenclature, and classify and characterize all the stable solutions to Eqs. (2), (6), and (8). Each stable solution corresponds to a specific director mode. In Refs. [12,13], we presented the following four planar solutions: (1) in-plane elastic driven steady state (IE), (2) in-plane tumbling wagging composite state (IT), (3) in-plane wagging state (IW), and (4) in-plane viscous driven steady state (IV); in this paper, we present the following out-of-plane modes: (5) out-of-plane elastic driven steady state with a chiral structure (OEA), (6) two out-of-plane elastic driven steady states with chiral structure [OEC[ $n$ ] ( $n = 1$  or 2)], (7) out-of-plane tumbling-wagging composite state with periodic emergence of a  $2\pi$  chiral structure (OTP), and (8) out-of-plane tumbling-wagging composite state with chiral structure (OTC). When  $R$  is large, the in-plane elastic driven steady state is similar but not identical to that predicted by the LE theory. When  $R$  and  $Er$  are sufficiently large, the bulk behavior (i.e., the  $y^* \approx 0.5$  region) of the three planar modes are similar but not identical to the Doi solutions of tumbling, wagging, and aligning states [7,8], while the behavior at the surface layers are characterized by (i) abnormal nematic state for IT mode, (ii) decreasing wagging amplitudes in the IW mode, and (iii) orientation boundary layers for the IV mode.

Figure 2 is a schematic of the rheological phase diagram given in terms of  $R$  and  $Er$ , clearly indicating the parametric regions where the four planar modes and the five nonplanar modes are stable. The figure shows the presence of eight regions, within which one, two, or four stable flow modes are predicted. The dashed line containing regions 2–5 denotes the parametric envelope within which the out-of-plane modes exist and are stable; outside the dashed line envelope (regions 1, 6, 7, and 8) only stable planar modes exist. If  $R$  is sufficiently low, stable nonplanar modes do not exist at any Ericksen number. If  $R$  is sufficiently high, the stable nonplanar modes share a boundary with the planar elastic-driven steady state mode (region 1) at lower  $Er$ , and with a time dependent tumbling-wagging composite mode (region 6) at high  $Er$  numbers. Thus out-of-plane modes arise when the  $R$  and  $Er$  numbers have significant magnitudes. The nine insets surrounding the sides and top of the rheological phase diagram are schematics of the main characterization of the director orientation profiles and the director dynamics. In the nine insets the director orientation is denoted by thick ar-

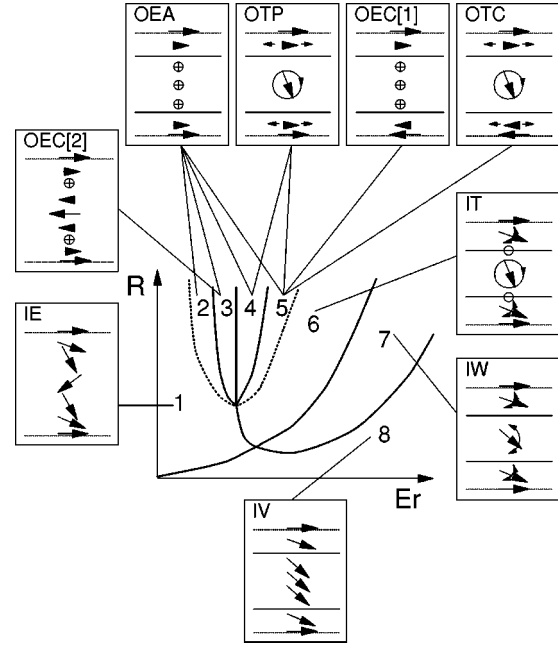


FIG. 2. Rheological phase diagram as a function of the ratio of short- to long-range elasticity ( $R$ ) and the ratio of viscous flow to long-range elasticity effects ( $Er$ ), and corresponding director configurations. There are eight flow regimes in the parametric space of  $Er$  and  $R$ , and nine flow modes. Lines represent flow regimes transitions. The dotted line shows the transition between in-plane and out-of-plane modes. The arrows represent the director, and the empty circles are the abnormal nematic state. See text.

rows, and the dashed lines denote the bounding surfaces ( $y^* = 0$  and 1); the fixed director surface orientation is denoted by the arrow lying on each dashed line. The symbol  $\oplus$  denotes a director orientation along the vorticity axis. The main features of the spatial distributions are that two modes (IE and OEC[2]) display one monotonic region behavior, while the other seven (IT, IW, IV, OEA, OEC[1], OTP, and OTC) display a boundary layer and bulk region behavior. In the latter the boundary layers are indicated by two thin lines parallel to the dashed lines. The dynamics of the director for the transient modes (IT, IW, OTP, and OTC) are indicated as follows: the double arrowheads represents director wagging (oscillations), and the full circle with an arrow represents director tumbling (rotation). The director orientation of the lower surface of the insets corresponding to OEC[1] and OTC shows that  $\mathbf{n} = (-1, 0, 0)$  and that the modes are chiral. The full twist shown in the inset for OEC[2] shows that this mode is also chiral. In addition, as shown below, the OTP mode exhibits periodic chirality.

Figure 3 shows the classification of the nine flow modes predicted by the complete theory for rectilinear shear start-up flow in terms of planar and nonplanar director orientations. The chart shows that planar modes can exhibit four types of transient (IW and IT) or steady state solutions (IE and IV). On the other hand, nonplanar modes show only an elastic-driven steady state (OEC, OEA) and tumbling-wagging composite (OTP, OTC) modes. However, the high dimensional director orientation generates director chirality, and the total number of the nonplanar flow modes is five.

The parameters and conditions that lead to the various solutions is explained in detail below. The main distinguish-

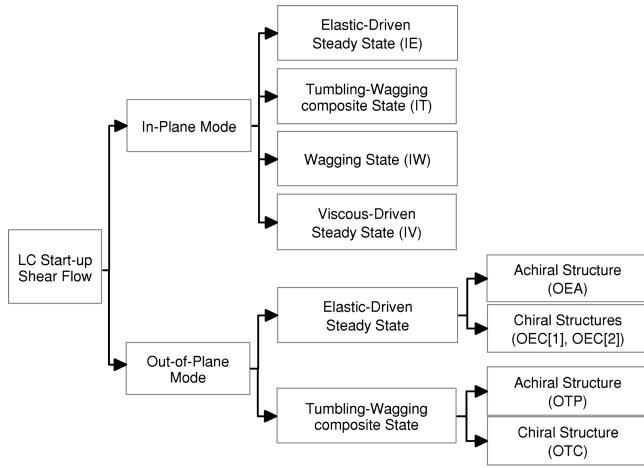


FIG. 3. Classification of flow modes in terms of dimensionality of director field (planar and nonplanar) and chiral properties of the director field (chiral structure and achiral structures). See text.

ing features of these nine flow modes are briefly summarized below. The solutions are naturally classified as in-plane modes (IE, IT, IW, and IV) and out-of-plane modes (OEA, OEC[ $n$ ], OTC, and OTP).

(1) In-plane elastic-driven steady state (IE)

The steady state of this planar mode arises due to the long range order elasticity stored in the deformed tensor order parameter field. In this planar mode there is no orientation boundary layer behavior, because there is no flow alignment in the bulk region.

(2) In-plane tumbling-wagging composite state (IT)

In this time dependent planar mode, the director dynamics in the bulk region is rotational and in the boundary layers it is oscillatory. The boundary between the bulk region and each boundary layers is characterized by the periodic emergence of the abnormal nematic state, which is characterized by two equal eigenvalues of the tensor order parameter (i.e.,  $\mu_n = \mu_m > \mu_l$ ), and allows for a smoothly defect-free transition from the rotational bulk region to the fixed director anchoring at the surfaces by a director resetting mechanism (see Ref. [12] for technical details).

(3) In-plane wagging state (IW)

In this planar mode, the director dynamics over the entire flow geometry is periodic oscillatory with an amplitude that decreases from a maximum at the centerline to zero at the two bounding surfaces.

(4) In-plane viscous-driven steady state (IV)

In this planar mode, the director profile shows a flow-aligning bulk region and two boundary layers. On traversing the boundary layers, the director rotates from the aligning angle to the flow direction at the walls [14].

(5) Out-of-plane elastic-driven steady state with achiral structure (OEA)

In this nonplanar mode, the director shows steady twist structures, and the twist angle profiles are symmetric with respect to the centerline. The steady state arises due to the long range order elasticity. Similar solutions were presented by the Leslie-Ericksen solutions [19–22]. On going for the bottom to top bounding surface, the net director twist rotation is nil.

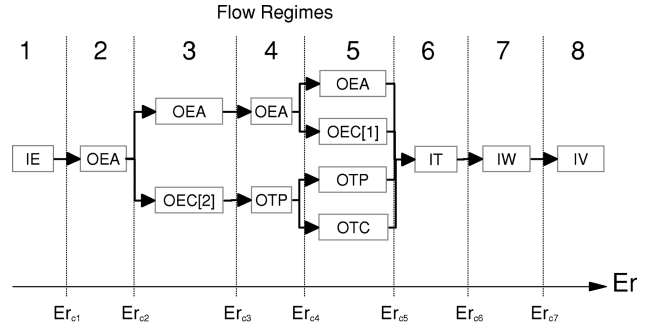


FIG. 4. Flow modes and eight regimes as a function of increasing Ericksen ( $Er$ ) number. Flow mode transitions occur at critical  $Er$  ( $Er_{ci}$ ,  $i=1, \dots, 7$ ). The out-of-plane regions (3, 4, and 5) exhibit solution multiplicity. With increasing  $Er$ , the in-plane modes are replaced by out-of-plane flow modes ( $Er_{c1}$ ), and eventually re-emerge at a high  $Er$  ( $Er_{c5}$ ) value.

(6) Out-of-plane elastic-driven steady state with chiral structure (OEC[ $n$ ])

In this nonplanar mode, the director shows steady twist structures, with an  $n\pi$  ( $n=1$  and  $2$ ) radian difference between the anchoring angles at the lower and upper bounding surfaces, but without the presence of defects or disclinations. The different anchoring conditions are smoothly connected by the chiral director structure. A similar OEC[2] solution is predicted by the Leslie-Ericksen equations [21].

(7) Out-of-plane tumbling-wagging composite state with periodic chirality (OTP)

In this nonplanar mode, the bulk director dynamics is planar and rotational, and in the two boundary layers is nonplanar oscillatory. The spatial profiles of the periodic director motion are antisymmetric. The director field exhibits periodic chirality; that is, after a cycle of  $2\pi$  chirality the director field enters a cycle of achirality, and thus after each  $2\pi$  rotation cycle of the bulk director the system periodically essentially recovers the spatially homogeneous director configuration [i.e.,  $\mathbf{n} \approx (1, 0, 0)$  for  $0 \leq y^* \leq 1$ ].

(8) Out-of-plane tumbling-wagging composite state with  $\pi$  chiral structure (OTC)

The director dynamics is in-plane rotational in the bulk region, and out-of-plane oscillatory in the boundary layers; the directors at the upper and lower bounding surfaces have opposite directions, and the system never recovers to the spatial homogeneous director configuration.

It is very important to characterize and understand the order in the emergence of the flow modes at sufficiently high  $R$  as a function of increasing Ericksen numbers. Figure 4 shows a schematic of the flow mode structure cascade as a function of increasing Ericksen numbers, where the symbols correspond to the solution modes described in this subsection. There are seven critical Ericksen numbers ( $Er_{ci}$ ,  $i=1, \dots, 7$ ), and eight flow regions which numbers correspond to those in Fig. 2. The out-of-plane flow modes exist in the intermediate regimes 2, 3, 4, and 5, while the in-plane modes exist at the low regime 1 and the higher regimes 6, 7, and 8. In the lowest  $Er$  region 1, the only solution is the IE flow mode. However, above certain critical  $Er_{c1}$ , instead of the stable in-plane flow mode, the OEA flow mode emerges. With further increase in  $Er$ , two stable solutions (OEA and OEC[2]) exist within the same Ericksen number interval (re-

gion 3). The OEC[2] solution becomes the OTP flow mode above  $Er_{c3}$  (region 4). In region 5, two more out-of-plane solutions (OEC[1] and OTC) arise in addition to OEA and OTP, and thus four stable out-of-plane solutions exist. At  $Er_{c5}$ , the four out-of-plane solutions cease to be selected, and the system exhibits the IT flow mode (region 6). Finally, regions 7 and 8 show IW and IV flow modes, respectively. The transitions and multistability of the flow modes are discussed in Sec. III C.

## 2. Classification of compatibility mechanisms between bulk director motion and fixed surface anchoring

In Ref. [12], it was discovered that the director rotation in the bulk region that exists for the director tumbling mode can be smoothly and continuously compatibilized with the fixed director at the bounding surfaces, through the periodic emergence of the abnormal nematic state. As mentioned above, the abnormal nematic state in two of the eigenvalues, i.e.,  $\mu_n = \mu_l$ , are equal, and thus the director is undefined and the spatially relative angle of the bulk director can be reset by  $\pi$  radians. In the present work we have discovered another compatibilizing mechanism between the bulk director rotation and the fixed surface anchoring. This additional compatibilizing mechanism is achieved by a nonplanar director temporal oscillation within the boundary layers (full details are given in Sec. III B).

While the dominant feature for the abnormal nematic state compatibilizing mechanism is the change in the scalar order parameter (eigenvalues of the tensor order parameter), for the out-of-plane director configuration compatibilizing mechanism it is the change in the director orientation (eigenvectors of the tensor order parameter). Depending on the parametric conditions (i.e., values of  $Er$  and  $R$ ), the system admits the order parameter or the director compatibilizing mechanisms. The scalar order parameter compatibilizing mechanism leads the system to the in-plane tumbling-wagging composite mode (IT flow mode), and the director compatibilizing mechanism leads the system to the out-of-plane tumbling-wagging composite state either with periodic chirality (OTP flow mode) or with  $\pi$  chiral structure (OTC flow mode). In addition, in certain regions of parametric space, both mechanisms appear during the initial transients.

### B. Out-of-plane solution modes (OEA, OEC[ $n$ ], OTP, and OTC modes)

In this section, we discuss in detail the structure of the out-of-plane solution modes (OEA, OEC[ $n$ ], OTP, and

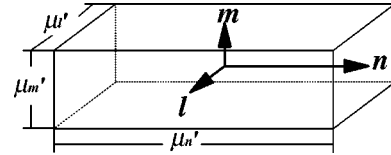


FIG. 5. Schematic of the utilized visualization of the tensor order parameter as a rectangular parallelepiped. The three eigenvalues and three eigenvectors of the order parameter tensor are simultaneously visualized. The three axes of the figure are parallel to the three eigenvectors of  $\mathbf{Q}$ , and the length of each edge is proportional to the three eigenvalues of  $\mathbf{Q}$ . For example, in the isotropic case, the parallelepiped becomes a cube.

OTC), which were briefly mentioned above. The exact nature of the mechanisms needed to achieve these flow modes will be discussed in Sec. III C. For direct visualization of the order parameter field  $\mathbf{Q}$ , we use a parallelepiped which makes possible the simultaneous presentation of the three eigenvectors ( $\mathbf{n}$ ,  $\mathbf{m}$ , and  $\mathbf{l}$ ) and three eigenvalues ( $\mu_n$ ,  $\mu_m$ , and  $\mu_l$ ). Figure 5 shows a schematic of the parallelepiped representing  $\mathbf{Q}$ ; the three axes of the figure are parallel to the three eigenvectors of  $\mathbf{Q}$ , and the longitude of each edge is proportional to the three eigenvalues of  $\mathbf{Q}$ . For example, in the isotropic case the parallelepiped becomes a cube. It should be mentioned that since the summation of the three eigenvalues is always zero, to draw the parallelepiped we apply a shift factor  $\alpha=0.53$  to the eigenvalues of  $\mathbf{Q}$ .

(A) Out-of-plane elastic-driven steady state with achiral structure (OEA)

This is a steady state flow mode that exists in regions 2–5 of the phase diagram (see Fig. 2). Figure 6 shows the scientific visualization of the tensor order parameter  $\mathbf{Q}$  as a function of dimensionless time  $t^*$  and dimensionless distance  $y^*$ , for  $Er=200$  and  $R=1000$  ( $De=0.2$ ). The director's escape from the shear plane appears close to both the upper and lower bounding surfaces at  $t^* \approx 15$ , and the out-of-plane front propagates toward the center line region. At  $t^* \approx 100$  the steady state has been reached, and the director field is characterized by a bulk region aligned along the vorticity axis and two boundary layers essentially aligned along the flow direction. The nature of the director's escape mechanism is the avoidance of the high free energy state, and thereby the director out-of-plane rotation occurs at the boundary layer close to the bounding surfaces where the gradient in the director field is highest. Once the out-of-plane orientation nucleates near the surface regions, it is easily transmitted to the bulk region by the long range elasticity.

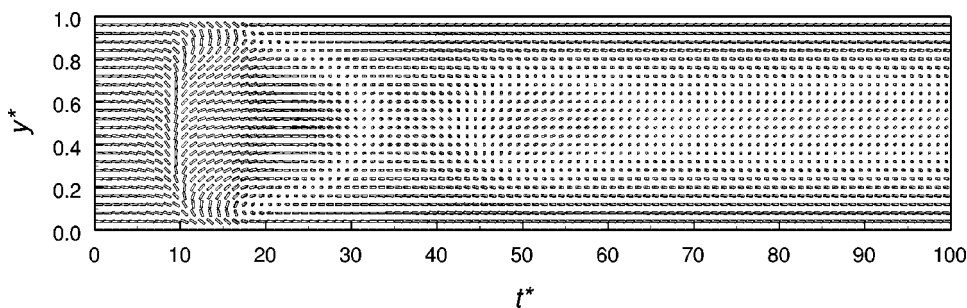


FIG. 6. Scientific visualization of the tensor order parameter as a function of dimensionless time ( $t^*$ ) and distance ( $y^*$ ), for  $Er=200$  and  $R=1000$  ( $De=0.2$ ). The figure shows the typical OEA flow mode at relatively low  $Er$ .

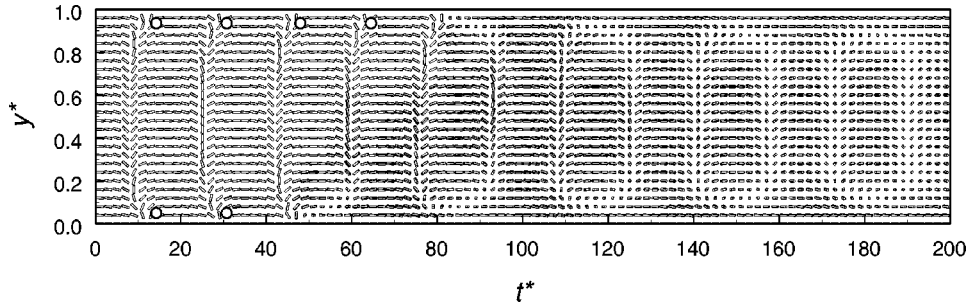


FIG. 7. Scientific visualization of the tensor order parameter as a function of dimensionless time ( $t^*$ ) and distance ( $y^*$ ), for  $Er = 1000$  and  $R = 1000$  ( $De = 1$ ). The empty circles represent the emergence of the abnormal nematic state. The figure shows the typical OEA flow mode at relatively high  $Er$ . The out-of-plane nucleation time increases with increasing  $Er$  (compare with Fig. 6).

The out-of-plane configuration reduces not only the director in-plane high gradient field, but also eliminates the rotational viscous flow effects. When the director is oriented parallel to the vorticity axis (the  $z$  axis), the flow has no rotational effect on the director, and thus the director is easily pinned down by the long range order elasticity. The boundary layer thickness containing the in-plane orientation decreases with increasing  $Er$ .

Figure 7 shows the computed scientific visualization of the order parameter tensor field as a function of dimensionless time  $t^*$  and dimensionless plates distance  $y^*$ , for  $Er = 1000$  and  $R = 1000$  ( $De = 1$ ). The circles in the figure represent the abnormal nematic states. The system entirely keeps the in-plane director profile until  $t^* \approx 45$ . For  $t^* \leq 45$ , the profile looks essentially like the in-plane tumbling-wagging composite (IT) mode (the abnormal nematic states appear close to both the upper and lower bounding surfaces at  $t^* \approx 13$  and 31). At  $t^* \approx 45$ , the transition from the in-plane mode to the out-of-plane mode nucleates close to the lower bounding surface, while the abnormal nematic state still appears close to the upper bounding surface. Then the out-of-plane configuration near the lower surface disappears, and the entire system almost (but not completely) recovers the in-plane homogeneous orientation profile at  $t^* \approx 68$ , and then at  $t^* \approx 80$  the out-of-plane mode nucleates near the upper bounding surface. After this early stage, that culminates with the in-plane to out-of-plane orientation mode transition, the director oscillates with decreasing amplitude, eventually

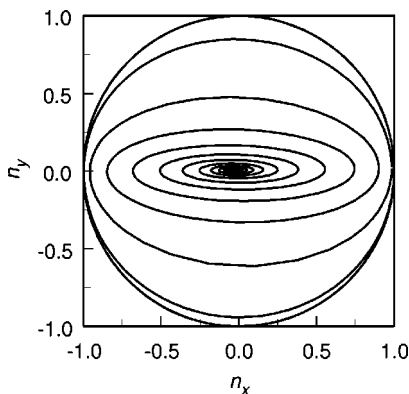


FIG. 8. Time trajectories of the director at the centerline ( $y^* = 0.5$ ), for  $Er = 1000$  and  $R = 1000$  ( $De = 1$ ), corresponding to Fig. 7. For the OEA flow mode the director eventually orients along the vorticity through damped oscillations.

reaching the steady out-of-plane profile.

Figure 8 shows the time trajectory of the director  $\mathbf{n}$  motion into the  $x$ - $y$  shear plane at the centerline ( $y^* = 0.5$ ), for  $Er = 1000$  and  $R = 1000$  ( $De = 1$ ), corresponding to Fig. 7. The director motion converges to the vorticity axis ( $x, y$ ) = (0, 0) with a damped rotational motion.

Figure 9 shows the steady spatial profiles of the out-of-plane twist angle  $\theta$  as a function of  $y^*$ , for  $Er = 200$  (solid line), 500 (dashed line), and 1000 (dotted line), and  $R = 1000$ . With increasing  $Er$ , the bulk region where the angle is close to zero becomes wider, and at sufficiently high  $Er$ , the mode is of boundary layer type. Han and Rey [22] reported a supertwisted out-of-plane director profile using the LE theory, while in the present work, the maximum deviation of the director from the shear plane is close to the  $\pi/2$  radians, and the supertwisted director configuration has not been observed. There are at least two possible reasons for the predicted maximum director angle. First, the viscous flow effect has a out-of-plane attractor along the vorticity axis [23]. In addition, the long range elasticity acts to reduce the spatial inhomogeneity of the tensor orientation field, and the inhomogeneity becomes higher with an in-plane director rotation, but lower with the out-of-plane rotation. Thus the long range elasticity also promotes orientation along the vorticity axis.

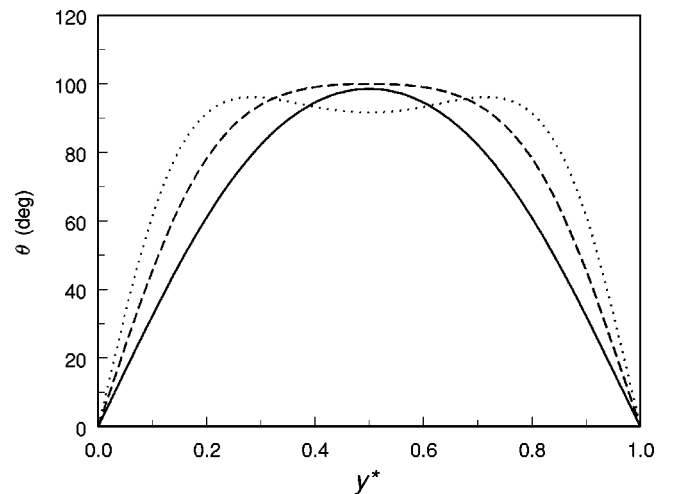


FIG. 9. Steady profiles of the director out-of-plane angle  $\theta$  as a function of  $y^*$ , for  $Er = 200$  (solid line), 500 (dashed line), and 1000 (dotted line), and  $R = 1000$ . All the profiles correspond to the OEA flow mode. As  $Er$  increases, the director bulk region where the angle  $\theta$  shows a plateau region of about  $90^\circ$  becomes wider.

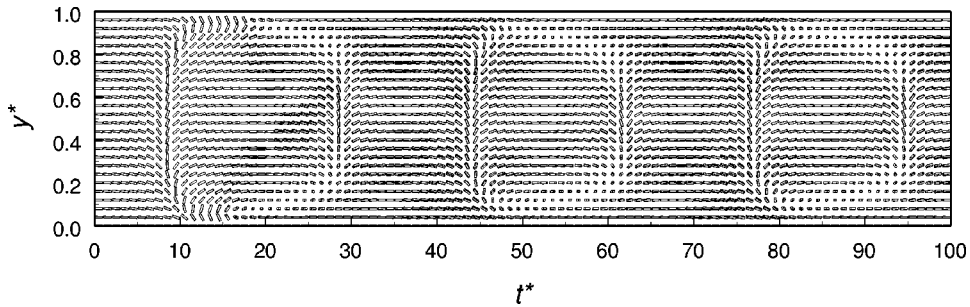


FIG. 10. Scientific visualization of the tensor order parameter as a function of dimensionless time ( $t^*$ ) and distance ( $y^*$ ), for  $Er = 1000$  and  $R = 1000$  ( $De = 1$ ). The figure shows the typical OTA flow mode at relatively low  $Er$ .

(B) Out-of-plane tumbling-wagging composite state with achiral structure (OTP)

The OTP mode is a time dependent periodic mode that exists in regions 4 and 5 of the phase diagram (see Fig. 2). A distinguishing characteristic is that it displays a tumbling in-plane core region and two wagging out-of-plane surface layers. In addition, the chirality of this mode is periodic, in which each achiral cycle is followed by a cycle in which the director profile has  $2\pi$  chirality. In the in-plane tumbling-wagging composite (IT) mode, the compatibility between the director tumbling in the bulk region and the fixed anchoring at the bounding surfaces is achieved by the periodic emergence of the abnormal nematic state [12]. In the abnormal nematic state, the director is undefined, and thus it is able to smoothly connect the tumbling director bulk region with the fixed director at the bounding surfaces. However, it is found that in the present out-of-plane OTP mode the compatibility between the bulk region and the fixed surface orientation is achieved without the periodic emergence of the abnormal nematic state, but instead through the wagging out-of-plane surface layers. The reason for this difference is that at lower  $Er$  long range elasticity is stronger, and promotes director compatibility modes, while at higher  $Er$  the flow is easily able to modify the scalar order parameters, and the compatibility is through the abnormal nematic state (order parameter mode).

Figure 10 shows the scientific visualization of the tensor order parameter field for  $Er = 500$  and  $R = 1000$  ( $De = 0.5$ ). As in the initial transients of the OEA flow mode, the out-of-plane orientation nucleates at points close to the bounding surfaces at  $t^* \approx 15$ , and then the out-of-plane front propagates toward the centerline. However, the out-of-plane component does not reach the centerline, and the bulk region near the centerline retains the in-plane tumbling (rotational) dynamics. The boundary layer regions close to the bounding surfaces shows out-of-plane wagging (oscillatory) behavior, known as kayaking-tumbling behavior [23]. When the bulk director rotates by  $\pi$  radians in the shear plane, the director in the bulk region  $\mathbf{n}_{\text{bulk}}$  and at bounding surfaces  $\mathbf{n}_y$  are antiparallel ( $\mathbf{n}_{\text{bulk}} = -\mathbf{n}_y$ ); this can be seen at  $t^* \approx 20, 55$ , and  $85$ . In principle, both in-plane and out-of-plane boundary layer configurations are possible to smoothly connect the two orientations. In the former case, the gradient in the director field increases with further rotation of the bulk director, unless the director resetting occurs by emergence of the abnormal nematic state, which is the mechanism adopted in the IT mode. In the latter case, however, the out-of-plane configuration recovers to the in-plane configuration after a further  $\pi$

rotation in the bulk region (i.e., the bulk director angle is  $2\pi$ ), and a homogeneous director profile results because  $\mathbf{n}_{\text{bulk}} = -(-\mathbf{n}_y)$ ; this can be seen in Fig. 10 at  $t^* \approx 37$  and  $70$ .

To demonstrate clearly the nature of the out-of-plane compatibilization mechanism which smoothly and continuously connects the director rotation in the bulk region to the fixed anchoring at the bounding surfaces, a time series of the computed spatial trajectories of the director  $\mathbf{n}$  spatial profiles (thick full and dashed lines) are shown in Figs. 11(a)–11(f), for  $Er = 500$  and  $R = 1000$  ( $De = 0.5$ ), corresponding to Fig. 10. The time conditions for the figures are (a)  $t^* = 0$ , (b)  $t^* = 10$ , (c)  $t^* = 15$ , (d)  $t^* = 20$ , (e)  $t^* = 25$ , and (f)  $t^* = 30$ . In the figure, dashed lines denote trajectories segments occluded from view. The filled square (■) denotes the centerline ( $y^* = 0.5$ ) orientation. At the  $t^* = 0$ , the trajectory is a point at  $(1, 0, 0)$  due to the essentially homogeneous director field. The point spreads, propagates clockwise along the equator [ $t^* = 10$ , Fig. 11(b)], and then the line splits into a closed ring due to the out-of-plane nucleation [ $t^* = 15$ , Fig. 11(c)]. At  $t^* = 20$  [Fig. 11(d)], the ring becomes almost a circle along the longitude, and this state represents the  $2\pi$  chiral structure of the director configuration. Through the  $2\pi$  twist configuration, the ring moves to the opposite side of the sphere (i.e.,  $y < 0 \rightarrow y > 0$ ), and eventually shrinks back to the initial point  $(1, 0, 0)$ . It is very important to emphasize that the director time trajectory at the centerline always shows a clockwise rotation on the equator (i.e., in-plane tumbling). The centerline in-plane tumbling is smoothly connected with the fixed anchoring condition [ $\mathbf{n} = (1, 0, 0)$ ], without any singularity or discontinuity, and when the bulk director rotates by  $2\pi$  radians the system almost recovers the homogeneous state. Thus the system periodically repeats the achiral-chiral structural change, corresponding to the  $2\pi$  in-plane rotation of the bulk director.

Figure 12 shows a scientific visualization of the tensor order parameter field for  $Er = 1000$  and  $R = 1000$  ( $De = 1$ ). Until  $t^* \approx 45$ , the bulk director rotation is connected with the fixed anchoring condition at the bounding surfaces through the scalar order parameter compatibilizing mechanism. At  $t^* \approx 45$ , the nonplanar orientation nucleates close to the lower plate, and then the gap between the bulk director rotation and the fixed anchoring at the lower plate is filled with the director compatibilizing mechanism. However, until the out-of-plane nucleates close to the upper plate at  $t^* \approx 80$ , the scalar order parameter compatibilizing mechanism is employed between the bulk director rotation and the fixed anchoring at the upper plate. Finally, for  $t^* > 80$ , the director

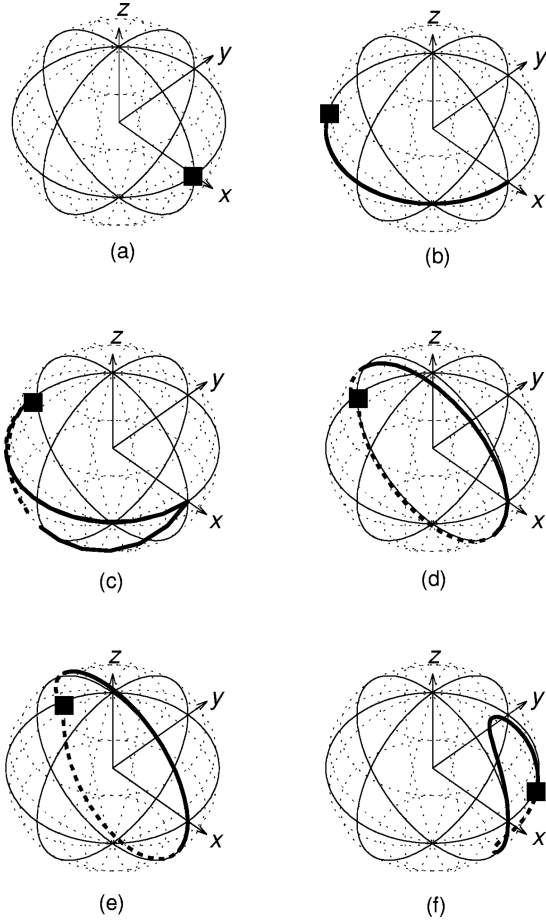


FIG. 11. Director spatial trajectories on the unit sphere, for  $Er = 1000$  and  $R = 1000$  ( $De = 1$ ): (a)  $t^* = 0$ , (b)  $t^* = 10$ , (c)  $t^* = 15$ , (d)  $t^* = 20$ , (e)  $t^* = 25$ , and (f)  $t^* = 30$ . The director motion on the equator is continuously and smoothly connected with the anchoring condition  $(1,0,0)$ , through the movement of a ringlike profile on the sphere. At  $t^* = 20$ , the trajectory is along the sphere's longitude, and this represents a director twist configuration with a  $2\pi$  chiral structure. See text.

compatibilizing mechanism appears at both lower and upper regions and the system adopts the OTP mode. It should be noted that the parametric conditions of Figs. 7 and 12 are identical ( $Er = 1000$  and  $R = 1000$ ), and this parametric condition corresponds to region 5 in Fig. 4. As mentioned above, within region 5 there are four possible solution modes. The

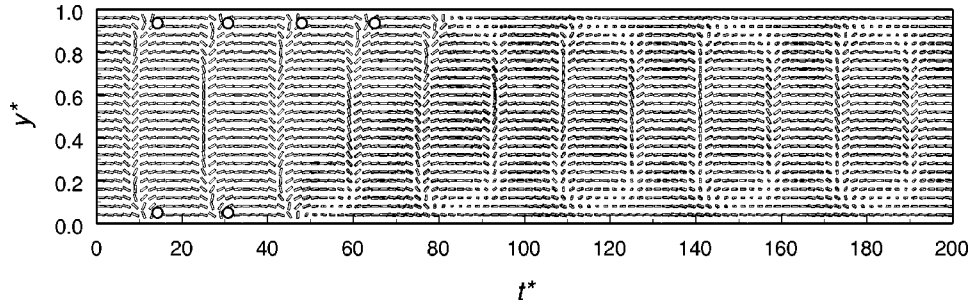


FIG. 12. Scientific visualization of the tensor order parameter as a function of dimensionless time ( $t^*$ ) and distance ( $y^*$ ), for  $Er = 1000$  and  $R = 1000$  ( $De = 1$ ). The empty circles represent the emergence of the abnormal nematic state. The figure shows the typical OTP flow mode at relatively high  $Er$ . The out-of-plane nucleation time increases with increasing  $Er$  (compare with Fig. 10). Note that the parametric condition is the same as Fig. 7 for the OEA flow mode, showing that the system exhibits multistability.

self-selection of the system flow mode is strongly dependent on the initial noise on the tensor field, although the noise amplitude is infinitesimally small. A full explanation of this multistability will be given in Sec. III C.

(C) Out-of-plane elastic-driven steady states with chiral structure (OEC[ $n$ ])

This is a steady state mode that exists in regions 3 and 5 of the phase diagram (see Fig. 2). As mentioned above,  $n$  shows the number of  $\pi$  rotations of the director angle, when going from the bottom bounding surface ( $y^* = 0$ ) to the top bounding surface ( $y^* = 1$ ). Thus the director twist  $\theta$  angle measured from the  $x$  direction satisfies:

$$\left| \int_0^1 \theta(y^*) dy^* \right| = n\pi. \quad (10)$$

In the case of an achiral structure,  $n = 0$ . In the present work, we found  $\pi$  and  $2\pi$  chiral structures for the OEC mode (regions 3 and 5 in Fig. 2).

Figure 13 shows the scientific visualization of the tensor order parameter field for  $Er = 120$  and  $R = 1000$  ( $De = 0.12$ ). The steady state solution is the OEC[2] mode. The out-of-plane tumbling nucleates close to the upper bounding surface at  $t^* \approx 21$ , and close to the lower bounding surface at  $t^* \approx 25$ , while the bulk directors try to retain the in-plane tumbling behavior. However, the rotational dynamics in the bulk are eventually quenched by the establishment of a  $2\pi$  chiral director structure. In the  $2\pi$  chiral director structure, the tilt angle  $\phi$  is nearly zero over entire flow regime at steady state. As shown in Fig. 2, the OEC[2] only occurs at lower Ericksen numbers (region 3 in Fig. 2), where the rotational viscous flow effect is relatively low. At  $t^* = 0$ , the long range elasticity effect, which is the driving force to achieve the steady state at low Ericksen numbers, is negligible, and thus the bulk director starts rotating, even though the director is nearly along the flow direction where the rotational speed is small. At steady state, the long range elasticity has a higher contribution than at  $t^* = 0$ , due to the spatially inhomogeneous  $2\pi$  chiral structure of the director configuration, and thus the long range elasticity contribution can balance the rotational viscous flow effect. If the Ericksen number is higher, the rotational viscous flow effect overcomes the long range elasticity effect, and the system cannot achieve a steady state, and it becomes an OTP flow mode. The  $2\pi$  chiral structure was also captured by Han and Rey

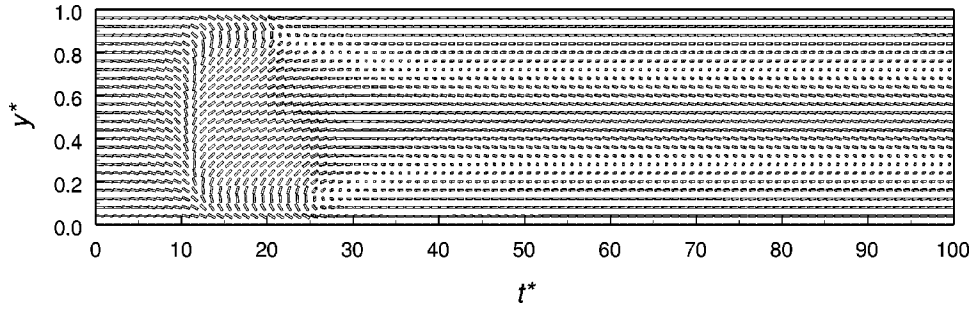


FIG. 13. Scientific visualization of the tensor order parameter as a function of dimensionless time ( $t^*$ ) and distance ( $y^*$ ), for  $Er = 120$  and  $R = 1000$  ( $De = 0.12$ ). The figure shows the typical OEC[2] flow mode. At the steady state of this state, the director field has a  $2\pi$  twist when going from upper to lower bounding surfaces.

[22] using the LE theory, but it arises through a different mechanism.

Figure 14 shows the scientific visualization of the order parameter field for  $Er = 1000$  and  $R = 1000$  ( $De = 1$ ). The solution is representative of the OEC[1] mode. After the early state of the in-plane tumbling mode, the out-of-plane orientation nucleates close to the lower bounding surface at  $t^* \approx 47$ . However, at the same time, close to the upper bounding surface the abnormal state emerges (see the circle in the figure). The director out-of-plane tumbling at the upper side of the flow geometry occurs at  $t^* \approx 65$ . The bulk director rotates  $\pi$  radians between  $t^* \approx 47$  and 65. At  $t^* \approx 52$ , while the orientation angle difference between the bulk director and the fixed director at the lower bounding surface is essentially  $\pi$  radians, the difference between the bulk director and the director at the upper bounding surface is almost zero. The net effect of the emergence of abnormal nematic state is to smoothly connect the bulk director orientation with the bounding surface for each  $\pi$  rotation of the bulk director. Furthermore, the fixed director at the bounding surface can be reoriented by the emergence of the abnormal nematic state either from  $\mathbf{n}_s$  to  $-\mathbf{n}_s$ , or  $-\mathbf{n}_s$  to  $\mathbf{n}_s$ . On the tensor order parameter level, there is no distinction between the head and tail of director, and its orientation is self-selected. At  $t^* \approx 45$ , while the upper side of the orientation field is homogenized due to the emergence of the abnormal nematic state, the lower side of the field shows the out-of-plane mode, and the bulk director and the director at the lower bounding surface are connected by the  $\pi$  chiral structure. The director at the upper bounding surface,  $\mathbf{n}_s^{\text{upper}}$ , is changed from  $(1,0,0)$  to  $(-1,0,0)$ , but at the lower bounding

surface it remains unchanged:  $\mathbf{n}_s^{\text{lower}} = (1,0,0)$ . Thus the system boundary condition switches from the parallel anchoring condition ( $\mathbf{n}_s^{\text{upper}} = \mathbf{n}_s^{\text{lower}}$ ) to the antiparallel anchoring condition ( $\mathbf{n}_s^{\text{upper}} = -\mathbf{n}_s^{\text{lower}}$ ), and this antiparallel director is smoothly connected with the twisted director configuration. The switching is self-selected. Since after the  $t^* \approx 45$  the abnormal nematic state never reappears, the antiparallel anchoring condition remains for all times. Keeping this structure, the bulk director saturates along the vorticity axis, and finally the system reaches a steady state with a  $\pi$  chiral director configuration.

(D) Out-of-plane tumbling-wagging composite state with chiral structure (OTC)

This is a time periodic mode that exists in region 5 of the phase diagram (see Fig. 2). In the OEC flow mode, there are two types of possible solutions (i.e.,  $n = 1$  and 2), as mentioned above. However, in the OTC flow mode, the  $\pi$  chiral ( $n = 1$ ) solution is the only solution.

Figure 15 shows the scientific visualization of the tensor order parameter field for  $Er = 1000$  and  $R = 1000$ . As in the OEC[1] flow mode, the  $\pi$  chiral structure is created due to the one sided emergence of the abnormal nematic state at  $t^* \approx 62$ . The mechanism to achieve the  $\pi$  chirality of the director configuration is exactly the same as it is for the OEC[1] mode. However, in the OTC mode, the bulk director retains the in-plane tumbling dynamics, and never attains a steady state. The director out-of-plane tumbling nucleates close to lower and upper bounding surfaces periodically and alternatively. For example, at  $t^* = 100$ , the out-of-plane exists around  $y^* = 0.1$ , and at  $t^* = 115$  it is around  $y^* = 0.9$ . It

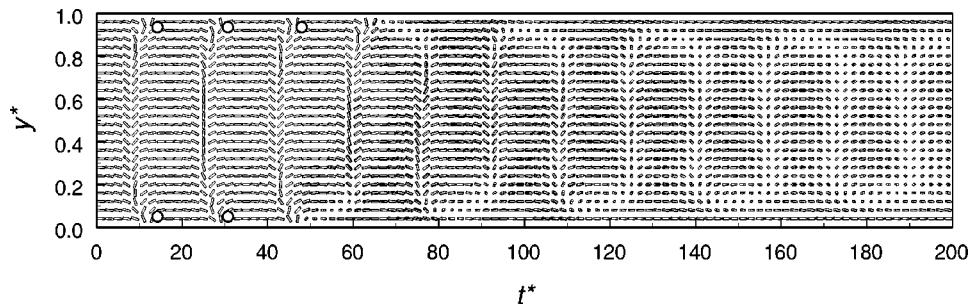


FIG. 14. Scientific visualization of the tensor order parameter as a function of dimensionless time ( $t^*$ ) and distance ( $y^*$ ), for  $Er = 1000$  and  $R = 1000$  ( $De = 1$ ). The empty circles represent the emergence of the abnormal nematic state. The figure shows the typical OEC[1] flow mode at relatively high  $Er$ . Note that the parametric condition is the same as Fig. 7 for the OEA flow mode, and Fig. 12 for OTP flow mode, thus showing that the system displays multistability.

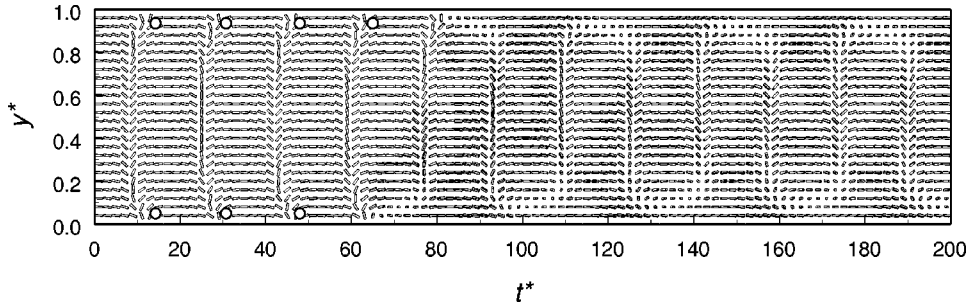


FIG. 15. Scientific visualization of the tensor order parameter as a function of dimensionless time ( $t^*$ ) and distance ( $y^*$ ), for  $Er = 1000$  and  $R = 1000$  ( $De = 1$ ). The empty circles represent the emergence of the abnormal nematic state. The figure shows the typical OTC flow mode at a relatively high  $Er$ . Note that the parametric condition is the same as Fig. 7 for the OEA flow mode, Fig. 12 for OTP flow mode, and Fig. 14 for the OEA[1] mode, thus showing that the system displays multistability.

should be noted that the chirality's sign at  $t^* = 100$  and  $115$  are opposite. At  $t^* = 100$ , the director exhibits counterclockwise  $\pi$  rotation in going from the lower to upper bounding surfaces, while at  $t^* = 115$  the director rotation is clockwise.

To characterize this chirality exchange, a time series of the spatial director trajectories corresponding to Fig. 15 is shown in Figs. 16(a)–16(i). The corresponding times are (a)  $t^* = 87$ , (b) 92, (c) 94, (d) 100, (e) 107, (f) 109, (g) 110, (h) 112, and (i) 115. The meaning of the dashed line and filled square are the same as in Fig. 11. The periodic emergence of the abnormal nematic state at only one surface layer causes the surface orientation exchange from parallel to antiparallel, such that  $\mathbf{n}_s^{\text{upper}} = (1, 0, 0) = -\mathbf{n}_s^{\text{lower}}$ . At  $t^* = 87$ , [Fig. 16(a)],

the two boundaries are connected with the longitude line passing through the north pole, showing the pure twisted director mode with a counterclockwise director rotation in going from the lower to upper bounding surfaces. Subsequently, in Figs. 16(b) and 16(c), a reverse orientation starts and propagates to the negative  $z$  and  $y$  face of the sphere, and when the reverse orientation reaches the top surface, the director trajectory is the longitude line passing through the south pole. The profile at  $t^* = 100$  [Fig. 16(d)] shows the pure twisted director configuration with clockwise director propagation from the lower to upper bounding surfaces, and thereby a chirality reversal of the director configuration is achieved smoothly and continuously. The clockwise director

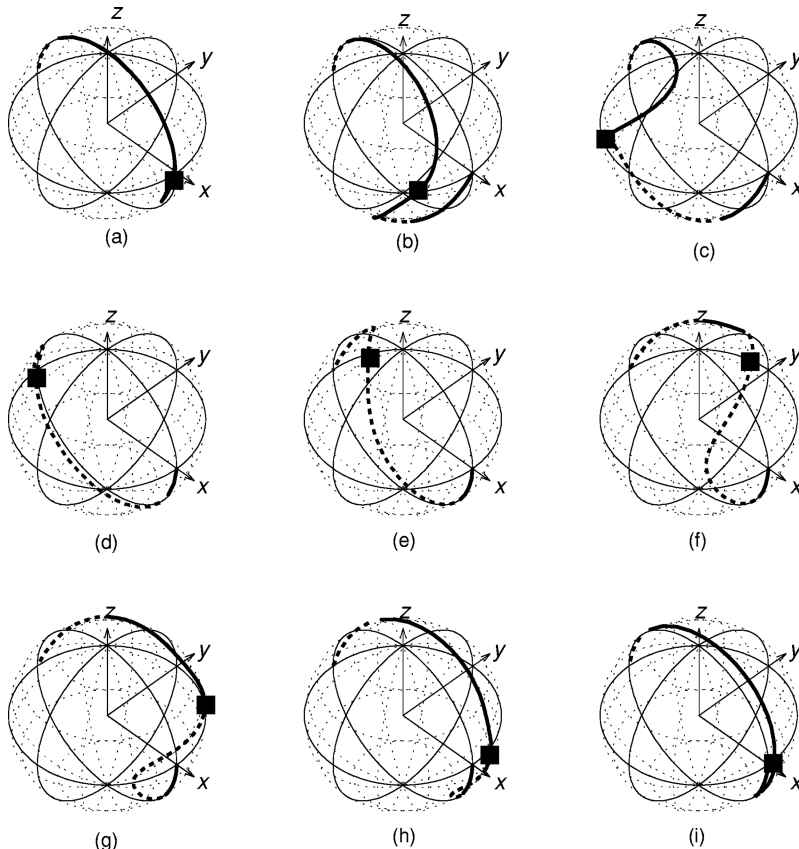


FIG. 16. Director spatial trajectories on the unit sphere, for  $Er = 1000$  and  $R = 1000$  ( $De = 1$ ): (a)  $t^* = 87$ , (b)  $t^* = 92$ , (c)  $t^* = 94$ , (d)  $t^* = 100$ , (e)  $t^* = 107$ , (f)  $t^* = 109$ , (g)  $t^* = 110$ , (h)  $t^* = 112$ , and (i)  $t^* = 115$ . The figure shows the typical OTC flow mode. Because of the  $\pi$  chiral structure of the system, the trajectories are anchored at  $(1, 0, 0)$  and  $(-1, 0, 0)$ .

TABLE I. Out-of-plane mode selection as a function of out-of-plane nucleation time [or  $\Delta m$  (difference in number of abnormal nematic states in the upper and lower surfaces)], and differences in the out-of-plane rotation sense.  $\Delta m = m^{\text{upper}} - m^{\text{lower}}$  is the difference between the number of abnormal nematic states that appear in the upper surface ( $m^{\text{upper}}$ ) and lower surface ( $m^{\text{lower}}$ ).

	Odd number of $\Delta m$	Even number of $\Delta m$
Same director rotation direction in the upper and lower surface regions	OTC mode	OEA mode
Different director rotation direction in the upper and lower surface regions	OEC mode	OTP mode

configuration recovers to the counterclockwise configuration (i) through the same procedure as from counterclockwise to clockwise, but through the opposite face of sphere [Figs. 16(e)–16(h)]. In the OTC mode, this jumping-rope-like profile evolution continues periodically.

### C. Solution multiplicity and probabilistic properties of the selection mechanisms

In Sec. III B, we presented four out-of-plane structures as well as discussed the transient processes that lead to their emergence. As shown in Figs. 2 and 4, in region 5 four out-of-plane solutions appear at the same parametric conditions. For example, for the parametric condition  $(Er, R) = (1000, 1000)$ , four stable flow modes (OEA, OTP, OEC[1], and OTC) may be selected with different probabilities. In the computational experiments, Eqs. (2), (6), and (8) are solved with different random seeds, so that the infinitesimal initial noise is different for each run; we have performed more than 20 runs for each parametric condition. From these results, it is found that the infinitesimal noise on the initial condition strongly affects the mode selection mechanism through the time and direction of the director's escape from the shear plane. The director can escape from the shear plane by a positive or negative twist, which decides whether the solution eventually adopts a steady state solution or a periodic solution. On the other hand, the chirality of the solution is decided by the out-of-plane nucleation time. It turns out that the out-of-plane nucleation time is directly related to the difference  $\Delta m$  in the number  $m^i$  ( $i$  is the upper or lower) of times that the abnormal nematic state emerges during the initial transients in the upper and lower surface layers,  $\Delta m = m^{\text{upper}} - m^{\text{lower}}$ . For example, in Figs. 7 and 12,  $m^{\text{upper}} = 4$  and  $m^{\text{lower}} = 2$ , and the out-of-plane nucleation times for the upper and lower regions are  $t_n^{\text{upper}} \approx 80$  and  $t_n^{\text{lower}} \approx 45$ ; in Fig. 14,  $m^{\text{upper}} = 3$ ,  $m^{\text{lower}} = 2$ ,  $t_n^{\text{upper}} \approx 65$ , and  $t_n^{\text{lower}} \approx 45$ ; and, in Fig. 15,  $m^{\text{upper}} = 4$ ,  $m^{\text{lower}} = 3$ ,  $t_n^{\text{upper}} \approx 80$ , and  $t_n^{\text{lower}} \approx 65$ . In what follows, we use out-of-plane nucleation time and  $\Delta m$  interchangeably. This noise controlled degree of freedom in the system dynamics occurs independently at the upper and lower surface regions. Table I shows the classification of the flow modes according to the director out-of-plane direction and  $\Delta m$ . The table shows that the four nonplanar flow modes

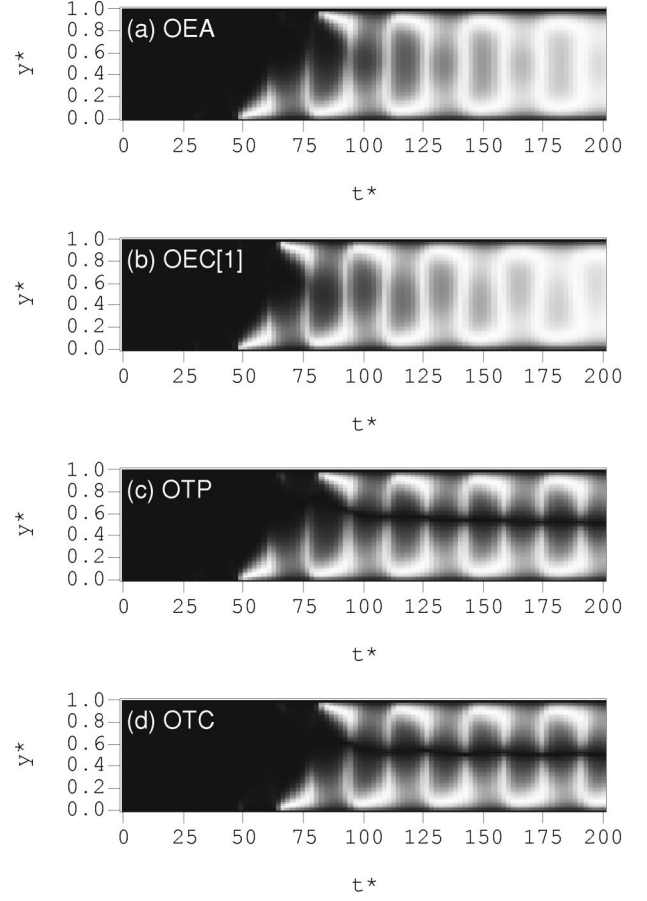


FIG. 17. Computed gray scale images of the out-of-plane component  $|n_z|$  typical of the four flow modes: (a) OEA, (b) OEC[1], (c) OTP, and (d) OTC. White:  $n_z = \pm 1$ ; black:  $n_z = 0$ . The parametric conditions are  $Er = 1000$  and  $R = 1000$  for all figures. These flow modes are caused by the coupling of the degrees of freedom in the director rotation direction and out-of-plane nucleation time. See text and Table I.

in region 5 of phase diagram (OEA, OEC[2], OTP, and OTC) are directly related to these two degrees of freedom.

The out-of-plane structures are shown in Figs. 17(a)–17(d) as gray scale images for the out-of-plane component  $|n_z|$  as a function of  $y^*$  and  $t^*$ , for the four out-of-plane modes, at  $Er = 1000$  and  $R = 1000$  ( $De = 1$ ). In the figure, black corresponds to planar orientation ( $n_z = 0$ ), and white to orientation along the vorticity axis ( $n_z = \pm 1$ ). Figure 17(a) is representative of the OEA flow mode. This mode shows closed ringlike out-of-plane wave propagation within an increasingly whiter background, indicating that eventually the bulk orientation is along the vorticity axis (see Fig. 2). Figure 17(b) is representative of the OEC[1] mode, and shows a square wave within an increasingly whiter background propagation, again indicating that eventually the bulk orientation is along the vorticity axis (see Fig. 2). Figure 17(c) is representative of the OTP mode, and shows permanent ringlike out-of-plane behavior with a dark band at the centerline, indicating that in-plane tumbling is always present in the bulk (see Fig. 2). Figure 17(d) is representative of the OTC mode, and is characterized by a square-wave-like permanent out-of-plane behavior with a dark band at the centerline, indicating that in-plane behavior is always present in the bulk (see Fig. 2).

The exact nature of the process leading to the selection of these modes in terms of relative twist rotation signs and out-of-plane nucleation time are as follows. The director out-of-plane rotation can be either positive or negative with equal probability. The resulting possibilities for the two surface regions are (1) both the upper and lower regions have a positive twist angle, (2) both have a negative twist angle, (3) the upper region has a positive twist angle and the lower region has a negative one, and (4) the upper region has a negative twist angle and the lower region a positive one. Due to mirror symmetry, cases (1) and (2), and cases (3) and (4), are equivalent. In the case that the upper and lower regions have the same director rotation direction [case (1) or (2)], and the fixed directors at the surfaces are the same [i.e.,  $\mathbf{n}_s^{\text{upper}} = \mathbf{n}_s^{\text{lower}}$ ], the bulk director also rotates out of plane in the same direction as the two boundary layers, and finally essentially aligns parallel to the vorticity axis where the rotational viscous flow effects vanish. As a result of this choice in escape mechanism and elimination of rotational flow torques, the system easily reaches the OEA steady state characterized by a bulk director aligned along the vorticity and two surface twisted layers. On the other hand, when the upper and lower regions have opposite director rotation directions [cases (3) and (4)], and the fixed directors at the surfaces are the same (i.e.,  $\mathbf{n}_s^{\text{upper}} = \mathbf{n}_s^{\text{lower}}$ ), the bulk director must pass through the shear plane at the centerline. Since the director is close to the shear plane, due to the strong rotational viscous torques the long term behavior displays periodic rotational director dynamics (OTP). However, when the fixed directors at the surfaces are opposite (i.e.,  $\mathbf{n}_s^{\text{upper}} = -\mathbf{n}_s^{\text{lower}}$ ), the relation between the director out-of-plane rotation direction and the system dynamics is different. When the upper and lower regions have the same director rotation direction and the fixed directors at the surfaces are opposite (i.e.,  $\mathbf{n}_s^{\text{upper}} = -\mathbf{n}_s^{\text{lower}}$ ), the system reaches a steady state, since the center of a  $\pi$  chiral director structure must pass through the vorticity axis at the centerline. When the upper and lower regions have different director rotation directions, and the fixed directors at the surfaces are opposite (i.e.,  $\mathbf{n}_s^{\text{upper}} = -\mathbf{n}_s^{\text{lower}}$ ), the system adopts a transient state with a tumbling bulk director.

Next we discuss the effect of the degree freedom in the out-of-plane nucleation time. Depending on the out-of-plane nucleation time, the number of abnormal nematic states during the transient process varies, and, as mentioned above, the abnormal nematic state is the major factor of the nucleation of  $\pi$  chirality. Both the abnormal nematic state and out-of-plane nucleation require high director gradients, and the system selects either the abnormal nematic state or the out-of-plane nucleation compatibilizing mechanism at the time where the director field has high gradients.

Figure 18 shows the schematic of the transient process that describes the transition from the in-plane mode to the out-of-plane mode for (a) the OTP mode, and (b) the OTC mode. The arrows represent the director orientation, the empty circles represent the abnormal nematic state, and the crossed circle the director orientation along the vorticity axis. The dynamics of the process have the following three distinctive stages (indicated below each schematic): (1) the early planar mode stage, during which abnormal nematic

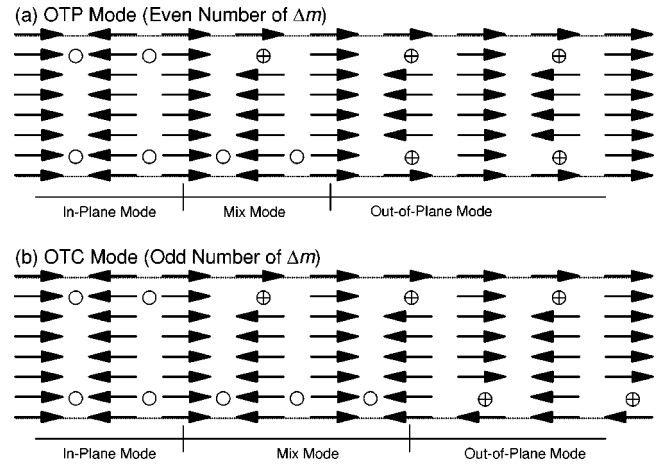


FIG. 18. Schematic of the system transient process from the in-plane mode to the out-of-plane mode, for (a) the OTP mode and (b) the OTC mode. The arrows show the director, and empty circles in the figures show the abnormal nematic state. Both the OTP and OTC modes have two transient processes and one final periodic state: (1) an initial in-plane flow stage; (2) an intermediate spatially in-plane and out-of-plane mixed flow stage, which connects the initial stage and the late stage; and (3) a late out-of-plane flow stage.

states appear at both surface layers; (2) the intermediate mix mode stage, during which both nonplanar orientation and abnormal nematic states appear at different surface layers; and (3) the late stage stable nonplanar mode. Here it should be emphasized that, as mentioned above, after each emergence of the abnormal nematic state, the fixed director at the bounding surfaces is reversed. In the OTP mode, the homogeneous director profile in the first column changes to the homogeneous reversed profile in the second column, since the bulk director rotates by  $\pi$  radians and both the upper and lower surface directors are reversed due to the emergence of the abnormal nematic states. Then, in the third column, the profile recovers to the almost same configuration as the first column through the same mechanism present in going from the first to second columns. However, in the fourth column, the  $\pi$  twisted director configuration appears. The lower surface director is reversed by the abnormal nematic state, but the upper director is not, since the out-of-plane nucleation arises at the upper region. In the fifth column, the homogeneous profile is achieved again, at which the bulk director orients along the same direction as the upper surface director through the  $\pi$  rotation, and the lower surface director is reversed to the same direction as the bulk director by the abnormal nematic state. Finally the out-of-plane nucleation also occurs in the lower region in the sixth column. The upper region also shows the out-of-plane twisted configuration, and the system shows the  $2\pi$  chiral structure at this stage. After the out-of-plane is nucleated at both upper and lower regions (i.e., after the system is totally transformed into the out-of-plane mode), the surface director reversing never occurs, and the system periodically shows the achiral and  $2\pi$  chiral structures. On the other hand, in the OTC mode, Fig. 18(b) shows the same process as the OTP mode until the fifth column of the director configuration. However, since the abnormal nematic state still appears between the fifth and sixth columns, the sixth column shows the  $\pi$  chiral

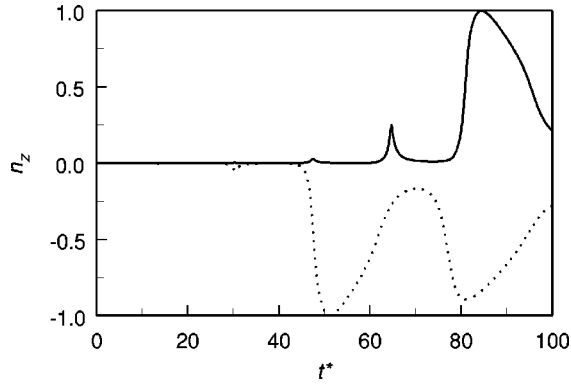


FIG. 19. Director out-of-plane component  $n_z$  as a function of dimensionless time ( $t^*$ ) at  $y^*=0.05$  (full line) and  $0.95$  (dashed line). The in-plane to out-of-plane transition occurs close to these spatial positions. The increasingly larger small peaks show the accumulation of  $n_z$ , eventually reaching a critical value at which the out-of-plane director escape occurs rapidly.

structure. The lower region out-of-plane nucleation occurs in the seventh column, and the lower surface director cannot recover to the same direction as the upper surface director anymore. As a result, the system permanently keeps the reversed surface directors, and the out-of-plane twisted profiles appear alternatively at the upper and lower regions. Since the one period of out-of-plane wagging is twice as long as that of in-plane tumbling, it directly shows that, for an even number of  $\Delta m$ , the upper and lower surface directors have the same direction (OTP mode), and for an odd number of  $\Delta m$  the directors have opposite directions and the system shows the  $\pi$  chiral structure (OTC mode).

Figure 19 shows the evolution of the director out-of-plane component  $n_z$  at  $y^*=0.05$  (dashed line) and  $y^*=0.95$  (full line), for  $Er=1000$  and  $R=1000$  ( $De=1$ ). The initial noise condition is the same as that used to find the solution shown in Fig. 11. Since the director rotation directions at  $y^*=0.05$  and  $0.95$  are opposite, the components have different signs. The absolute values of  $n_z$  display a train of pulses whose amplitudes increase with increasing time. Comparing with Fig. 11, the peaks correspond to the emergence of the abnormal nematic state. At the small peaks, the abnormal nematic state emerges instead of the out-of-plane mode. After each peak, the out-of-plane component decays but does not recover to zero, and the residual out-of-plane mode accumulates more and more after each successive pulse. Eventually the accumulated twist exceeds a critical value, and it rapidly grows toward its maximum value ( $n_z = \pm 1$ ). Before the out-of-plane nucleation occurs, the abnormal nematic emerges four times in the upper region and twice in the lower region. Since the accumulation is small and slow in the early stage, the infinitesimal noise can directly affect the process. As a result of the noise effect, even if the equation is deterministic and the noise on the initial condition is infinitesimally small, the in-plane to out-of-plane transition is stochastic. As mentioned above, the most important effect of this stochastic transition occurrence time is its control of the chirality. Thus the system chirality also arises stochastically.

The number of abnormal nematic states during the transient process (or, equivalently, the out-of-plane nucleation time) is strongly affected by the Ericksen number. Figure 20

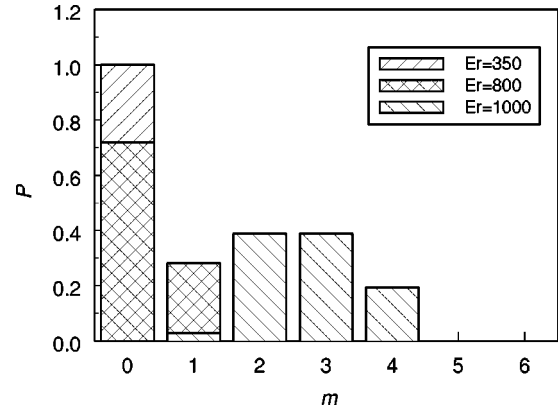


FIG. 20. Probability distribution  $P$  of the number  $m$  of the abnormal nematic state that emerges before the out-of-plane nucleation, for  $Er=350$ ,  $800$ , and  $1000$ . For  $Er=350$ , the transition always occurs at  $m=0$ , and the distribution becomes wider and its peak position moves to higher  $m$  as  $Er$  increases.

shows the probability distribution of the number of abnormal nematic states for  $Er=350$ ,  $800$ , and  $1000$ , and  $R=1000$ . As  $Er$  decreases, the distribution becomes narrow, and its peak position tends to  $m=0$ . When  $Er=350$ , there is no freedom in the out-of-plane nucleation time. As  $Er$  increases, the director's escape from the shear plane slows down because the in-plane flow attractor [23] tries to suppress the out-of-plane component accumulation process described in Fig. 19, and above a certain critical  $Er$  the flow attractor prevails over the out-of-plane attractor and the system changes to the in-plane flow mode. At a relatively lower  $Er$ , the system has only achiral structures, except the OEC[2] mode, since both  $m^{\text{upper}}$  and  $m^{\text{lower}}$  are always equal to 1. This distribution is used to compute the observation probability of the four out-of-plane (OTC, OEA, OEC, and OTP) modes. Table II shows the observation probability as a function of the Ericksen number for even numbers and odd numbers of  $\Delta m$ . As  $Er$  increases, beyond the critical value of 500, the probability of chirality increases from zero to 50% at  $Er=1000$ . As  $Er$  decreases, the observation probability for an odd mode continuously decreases to zero, and thus the system continuously decreases the degree of solution multiplicity, eventually entering the achiral region 4 (see Fig. 2).

Finally, observation probabilities of all the flow modes for all the flow regimes are shown in Fig. 21. In this figure, the probabilities are plotted for each flow mode, and thus for any Ericksen number the sum of the probability is 1. For ex-

TABLE II. Observation probability for chiral and achiral modes as a function of the Ericksen number.  $Er$ : Ericksen number;  $\Delta m = m^{\text{upper}} - m^{\text{lower}}$ : difference between the number of abnormal nematic states that appear in the upper surface ( $m^{\text{upper}}$ ) and in the lower surface ( $m^{\text{lower}}$ ).

	Observation probability of even number of $\Delta m$ (achiral)	Observation probability of odd number of $\Delta m$ (chiral)
$Er=500$	100%	0%
$Er=800$	60%	40%
$Er=1000$	51%	49%

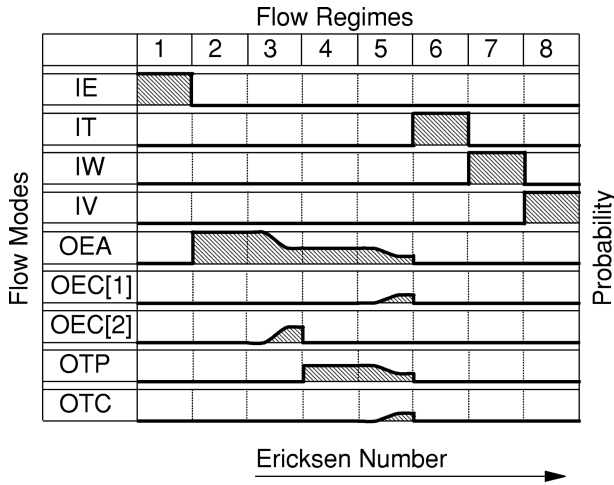


FIG. 21. Flow mode observation probability as a function of the Ericksen number. The figure presents the concept of flow regime transitions in terms of the change in the observation probability with increasing  $Er$ . For example, the smooth change in the observation probability causes the transitions from regime 2 to 3, and also from regime 4 to 5. See text.

ample, for region 1 the probability of an IE mode is 1 and others are zero, and for region 4 the probability of OEA and OTP flow modes are almost 0.5, and the others are zero. The reason for the transition between regimes 2 and 3 arises from the loss of freedom in the director rotation direction. The boundary layer thickness increases with decreasing  $Er$ , and thus the two out-of-plane nucleation points become closer. When the points come closer than a certain correlation length, their rotation directions are also restricted by each other, and then the system loses the OEC[2] flow mode and changes from regime 3 to regime 2 (see Fig. 2). It is important to emphasize that, as mentioned in Sec. II, all the simulations we performed using the initial condition given by Eqs. (9a) and (9b), and that the selected stable flow modes for a specific set of parametric conditions are those shown in Fig. 21.

#### D. Rheological phase diagram

At this stage we are now able to present a more technical description of the phase diagram, shown in Fig. 2. In Ref. [13], Tsuji and Rey reported a rheological phase diagram for the in-plane case, where no out-of-plane modes are included. Since the stochastic data require a huge computational task, we have not found the exact transition lines. The approximate locations of the transition lines, including the out-of-plane flow modes, are adopted from extensive computational results. From the structure of Fig. 2, one can see that the out-of-plane flow regimes are superimposed over the higher Ericksen number IE regime and the lower Ericksen number IT regime. The high gradient in the orientation field can be achieved at the high Ericksen number region in the IE flow mode, and also all over the IT flow regime. At the high Ericksen number region in the IT flow mode, as mentioned above, the in-plane attractor of the viscous flow, which increases with increasing  $Er$ , prevails over the out-of-plane attractor by the long range elasticity. The out-of-plane flow regimes appear above a certain  $R$ , and the interval of  $Er$  on

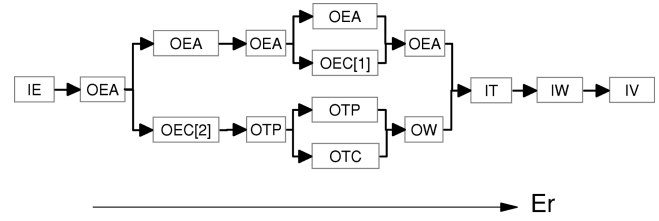


FIG. 22. Organization of flow modes for high elastic anisotropy. The out-of-plane flow regime is wider and spreads into the wagging regime, when compared to that for lower elastic anisotropy (see Fig. 4). Higher elastic anisotropy promotes out-of-plane flow modes by a reduction of long range elasticity.

which they are found becomes wider with increasing  $R$ . Because  $R$  is the ratio of the short range to the long range elasticity, if  $R$  is high, the system tends to keep the equilibrium scalar order parameter. The in-plane tumbling-wagging composite flow mode is allowed through the periodic emergence of an abnormal nematic state, where the scalar order parameter decreases by the high gradient in the director field through the long range order elasticity, and thus this mode requires a low  $R$  or a strong in-plane attractor. In other words, at high  $R$  the short range elasticity also help the director to escape from the shear plane to minimize the change in the scalar order parameter, and a stronger in-plane attractor is needed to retain the director in the shear plane.

#### E. Effect of elastic anisotropy

To examine the effect of the elastic anisotropy on the out-of-plane phenomena, computations have been performed with different values of the elastic anisotropy ratio  $e$ :

$$e = \frac{L_2}{L_1}.$$

Two representative cases,  $e=0$  and 9, are chosen for low and high elastic anisotropy. The case  $e=0$  corresponds to isotropic elasticity (i.e.,  $K_1=K_2=K_3$ ), and  $e=9$  corresponds to  $K_1=K_3=10K_2$ , in the limit of uniaxial nematic ordering. It is well known that the ratio of  $K_2$  to  $K_1$  is the most effective parameter for the director out-of-plane phenomena, since the out-of-plane phenomena are caused by the lower energy of the director twisted configurations. Thus it is obvious that the out-of-plane phenomena easily occur for higher  $e$ , while for lower  $e$  the energy reduction by the scalar order parameter may be easily employed by the system.

It is found that for  $e=9$  the out-of-plane flow regime spreads to the higher Ericksen number; the out-of-plane to in-plane transition occurs in the IW regime. As a result of this spreading of the out-of-plane regime, the out-of-plane wagging flow mode appears, in addition to the flow modes for  $e=9$ . The structure of the flow modes with increasing  $Er$  is shown in Fig. 22, for the high elastic anisotropic case ( $e=9$ ). Energy reductions caused by the director's escape from the shear plane become larger with increasing  $e$ , and a higher  $Er$  is required to retain the director within the shear plane. In the lower Ericksen number IW regime, the bulk director periodically has an angle almost orthogonal to the flow direction, and this angle (or the gradient in the orientation field at the boundary layer) becomes smaller with in-

creasing  $Er$ . When the angle becomes small enough and the viscous flow in-plane attractor becomes strong enough, the system changes into the in-plane flow mode.

Intuition would suggest that in the case of isotropic elasticity, the elastic driving force for director escape from the shear plane should not exist. However, the in-plane to out-of-plane transition is also confirmed for  $e=0$ . While the accumulated maximum angle of the bulk planar director with respect to the fixed surface orientation should increase without bounds at certain extreme parametric conditions, the maximum out-of-plane director angle is at most  $\pi/2$ . Also, by achieving the out-of-plane configuration, the system can avoid the abnormal nematic state which increases the system's energy at high  $R$ . Thus it is expected that with decreasing  $e$  the out-of-plane flow regime becomes narrower, and a higher  $R$  is required to achieve the out-of-plane flow mode. These findings clearly show that elastic anisotropy is not always necessary to promote the emergence of nonplanar shear flow modes.

#### IV. CONCLUSIONS

In this paper, we have performed an extensive analysis of the flow orientation structure of liquid crystalline materials, using a complete nonlinear tensor theory. The one-dimensional rectilinear simple shear start-up flow was fully characterized for unrestricted self-selected 3D orientation fields.

In addition to four in-plane flow modes IE, IT, IW, and IV, five out-of-plane flow modes (OEA, OEC[1], OEC[2], OTP, and OTC) are found in the parametric space which is spanned by  $R$  (the ratio of short range order elasticity to long range elasticity) and  $Er$  (the ratio of viscous force to long range elastic force). The OEA mode is a steady state at which the steady twist angle profiles are symmetric with respect to the centerline, and arises due to the long range order elasticity, like the LE out-of-plane solutions. The OEC[ $n$ ] modes are also steady states, where the director shows steady twist structures, with an  $n\pi$  ( $n=1$  and  $2$ ) radian difference between the anchoring angles at the lower and upper bounding surfaces. These structures are created without the presence of defects or disclinations. The OTP is a periodic state at which the director dynamics is planar rotational in the bulk region, and nonplanar oscillatory in the two boundary layers. The director field exhibits the periodic emergence of  $2\pi$  chirality. The OTC is a periodic state where the director dynamics is in-plane rotational in the bulk region and out-of-plane oscillatory in the boundary layers. The major difference from the OTP mode is that the directors at the upper and lower bounding surfaces have opposite directions, and the system never recovers the spatial homogeneous director configuration.

The proliferation of flow modes is due to the fact that there are two mechanisms to compatibilize the bulk director rotation to the fixed director at the bounding surfaces: (i) by changing the scalar order parameter, and (ii) by changing the director orientation. The former compatibilization mechanism is adopted by the IT mode, and causes the director resetting mechanism through the abnormal nematic state. On the other hand, the latter compatibilization mechanism leads the system either to the OTP mode or to the OTC mode, where the mechanism appears as the out-of-plane wagging at the boundary layers. As clearly shown in the rheological phase diagram (Fig. 2), the selection of the compatibilization mechanism depends on the parametric conditions.

Multistabilities and stochasticity of the flow modes are found in the out-of-plane flow regimes. The flow mode selection at the multistable regimes is strongly coupled with degrees of freedom in the director dynamics: (i) the director out-of-plane rotation direction, and (ii) the out-of-plane nucleation time. The rotation direction controls the system dynamics (steady state or periodic state), and the nucleation time controls the system chirality. The maximum number of multistable solutions are clearly explained in terms of the coupling of these two degrees of freedom. Also, the transitions between the out-of-plane flow regimes are well established with the probability of these degrees of freedom. In other words, the loss of these degrees of freedom causes the transitions.

High anisotropy in the long range elasticity causes the spread of the out-of-plane flow regimes, and causes other flow modes such as the out-of-plane wagging state. On the other hand, isotropic elasticity results in narrower  $Er$  intervals on which out-of-plane regimes exist, but the nonplanar modes nevertheless exist.

The complete tensor theory [12] is based on a unification of the classical nonequilibrium theories of liquid crystals, already used by de Gennes [1] to describe the nonequilibrium isotropic phase of a nematic liquid crystal under shear. The predictions of the complete theory transcend the nature of the flow, and the transitions predicted by the classical theories. The transcendence is reflected by the emergence of transient chiral modes, transient out-of-plane rotational modes, and mixed planar-nonplanar modes, and by the stochastic nature of out-of-plane mode selection. These findings are being used to explain the ubiquitous pattern formation processes of nematic liquid crystalline materials under flow.

#### ACKNOWLEDGMENTS

One of us (A.D.R) gratefully thanks the Natural Science and Engineering Research Council in Canada for their financial support. Also, we would like to thank Dr. W. H. Han (NIST) for the useful discussion on the  $2\pi$  chiral structure creation of the LE model.

- 
- [1] P. G. de Gennes, *The Physics of Liquid Crystals* (Clarendon, Oxford, 1974).  
 [2] F. C. Frank, *Discuss. Faraday Soc.* **25**, 19 (1958).  
 [3] F. M. Leslie, *Theory of Flow Phenomena in Liquid Crystals, Advances in Liquid Crystals* (Academic, New York, 1979), p. 1.

- [4] M. Doi, *J. Polym. Sci., Polym. Phys. Ed.* **19**, 229 (1981).  
 [5] T. Carlsson, *Mol. Cryst. Liq. Cryst.* **104**, 307 (1984).  
 [6] A. D. Rey and M. M. Denn, *J. Non-Newtonian Fluid Mech.* **27**, 375 (1988).  
 [7] G. Marrucci and F. Greco, *Adv. Chem. Phys.* **LXXXVI**, 331 (1993).

- [8] R. G. Larson, *Macromolecules* **23**, 3983 (1990).
- [9] S. Chandrasekhar, *Liquid Crystals* (Cambridge University Press, Cambridge, 1977).
- [10] R. G. Larson, in *Spatio-Temporal Patterns in Nonequilibrium Complex Systems*, edited by P. E. Cladis and P. Palfy-Muhoray (Addison-Wesley, Reading, MA, 1995), p. 219.
- [11] H. Fischer, A. Keller, and A. H. Windle, *J. Non-Newtonian Fluid Mech.* **67**, 241 (1996).
- [12] T. Tsuji and A. D. Rey, *J. Non-Newtonian Fluid Mech.* **73**, 127 (1997).
- [13] T. Tsuji and A. D. Rey, *J. Non-Newtonian Fluid Mech.* (to be published).
- [14] A. Sonnet, A. Kilian, and S. Hess, *Phys. Rev. E* **52**, 718 (1995).
- [15] W. H. Han and A. D. Rey, *Phys. Rev. E* **49**, 597 (1994).
- [16] P. Pieranski and E. Guyon, *Phys. Rev. Lett.* **32**, 924 (1974).
- [17] M. Srinivasarao, *Int. J. Mod. Phys. B* **9**, 2515 (1995).
- [18] M. Srinivasarao and G. Berry, *J. Rheol.* **35**, 379 (1991).
- [19] I. Zuniga and F. M. Leslie, *Liq. Cryst.* **5**, 725 (1989).
- [20] I. Zuniga and F. M. Leslie, *J. Non-Newtonian Fluid Mech.* **33**, 123 (1989).
- [21] W. H. Han and A. D. Rey, *J. Non-Newtonian Fluid Mech.* **48**, 181 (1993).
- [22] W. H. Han and A. D. Rey, *Phys. Rev. E* **50**, 1688 (1994).
- [23] R. G. Larson and H. C. Ottinger, *Macromolecules* **24**, 6270 (1991).
- [24] N. C. Andrews, A. J. McHugh, and B. J. Edwards, *J. Rheol.* **40**, 459 (1996).
- [25] M. J. Stephen and J. P. Straley, *Rev. Mod. Phys.* **46**, 617 (1974).
- [26] A. D. Rey, *Macromol. Theory Simul.* **4**, 857 (1995).
- [27] A. D. Rey, *Macromolecules* **24**, 4450 (1991).
- [28] N. C. Andrews, B. J. Edwards, and A. J. McHugh, *J. Rheol.* **39**, 1161 (1995).